

Above and beyond: Holographic tracking of axial displacements in holographic optical tweezers

Michael J. O'Brien and David G. Grier

*Department of Physics and Center for Soft Matter Research,
New York University, New York, New York 10003, USA*

How far a particle moves along the optical axis in a holographic optical trap is not simply dictated by the programmed motion of the trap, but rather depends on an interplay of the trap's changing shape and the particle's material properties. For the particular case of colloidal spheres in optical tweezers, holographic video microscopy reveals that trapped particles tend to move farther along the axial direction than the traps that are moving them and that different kinds of particles move by different amounts. These surprising and sizeable variations in axial placement can be explained by a dipole-order theory for optical forces. Their discovery highlights the need for real-time feedback to achieve precise control of colloidal assemblies in three dimensions and demonstrates that holographic microscopy can meet that need.

INTRODUCTION

Holographic optical traps use the forces and torques exerted by computer-generated holograms to localize and manipulate micrometer-scale objects [1, 2]. In principle, holographic traps can move colloidal particles along arbitrary paths in three dimensions and can arrange multiple particles into precisely specified three-dimensional configurations [3–5]. In practice, however, where a trap places a particle depends on details of the particle's interaction with the light field. Here, we use Lorenz-Mie microscopy to measure colloidal spheres' trajectories in holographic traps and thereby to demonstrate that particles with different sizes and compositions not only reside at different axial positions within coplanar traps, but indeed travel substantially different distances when the traps are displaced along the optical axis. This surprising observation can be explained by considering how an optical trap's structure depends on its axial position. Even so, axial displacements pose a practical challenge because variations from particle to particle can be large and are difficult to predict quantitatively. We demonstrate that Lorenz-Mie microscopy can provide the real-time feedback needed to achieve precise three-dimensional control over colloidal assemblies with holographic optical traps.

HOLOGRAPHIC OPTICAL TRAPPING

The holographic trapping technique, depicted schematically in Fig. 1(a), uses computer-generated holograms to structure the wavefronts of a laser beam so that the modified beam forms the desired configuration of optical traps when brought to a focus by a strongly converging objective lens [1, 2]. The implementation used for this study is driven by a 10 W fiber laser (IPG Photonics, YLR-10-LP) operating at a vacuum wavelength of $\lambda_0 = 1064$ nm. Holograms are imprinted on this laser's wavefronts using a liquid-crystal spatial

light modulator (Holoeye Pluto). The modified beam is then projected into the sample by a $100\times$ oil-immersion objective lens with a focal length of $f = 200$ μm and a numerical aperture of $\text{NA} = 1.4$. (Nikon S-Plan Apo).

The ideal scalar hologram encoding N point-like optical tweezers [6, 7],

$$E(\boldsymbol{\rho}) = \sum_{j=1}^N E_j \exp\left(-i\frac{k}{f} \mathbf{r}_j \cdot \boldsymbol{\rho}\right) \exp\left(i\frac{k}{2f^2} z_j \rho^2\right), \quad (1)$$

places the j -th trap at position \mathbf{r}_j relative to the center of the objective's focal plane at $z = 0$. Here, $\boldsymbol{\rho}$ is the two-dimensional coordinate of a point in the hologram plane, $k = 2\pi n_m/\lambda_0$ is the light's wavenumber in a medium of refractive index n_m , and E_j is the complex amplitude of the j -th trap. The total power required to project this pattern is

$$P = \frac{1}{2} \Omega n_m c \epsilon_0 \sum_{j=1}^N |E_j|^2, \quad (2)$$

where c is the speed of light in vacuum, ϵ_0 is the vacuum permittivity, and Ω is the effective cross-sectional area of the projection system. The example hologram in Fig. 1(a) encodes the phase profile,

$$\varphi(\boldsymbol{\rho}) = \frac{k}{2f^2} z_j \rho^2 \text{ mod } 2\pi, \quad (3)$$

of a single optical tweezer displaced by z_j along the optical axis.

Equation (1) can be generalized to project line traps [8, 9], ring traps [10, 11], knotted traps [11, 12] and tractor beams [13, 14], among many other modalities. Hardware-accelerated algorithms can perform the necessary field calculations in real time, permitting dynamic interaction with trapped materials [15].

Although the focal point of a trap may be located at \mathbf{r}_j , the point of mechanical equilibrium for a particle localized in the trap typically is displaced by radiation

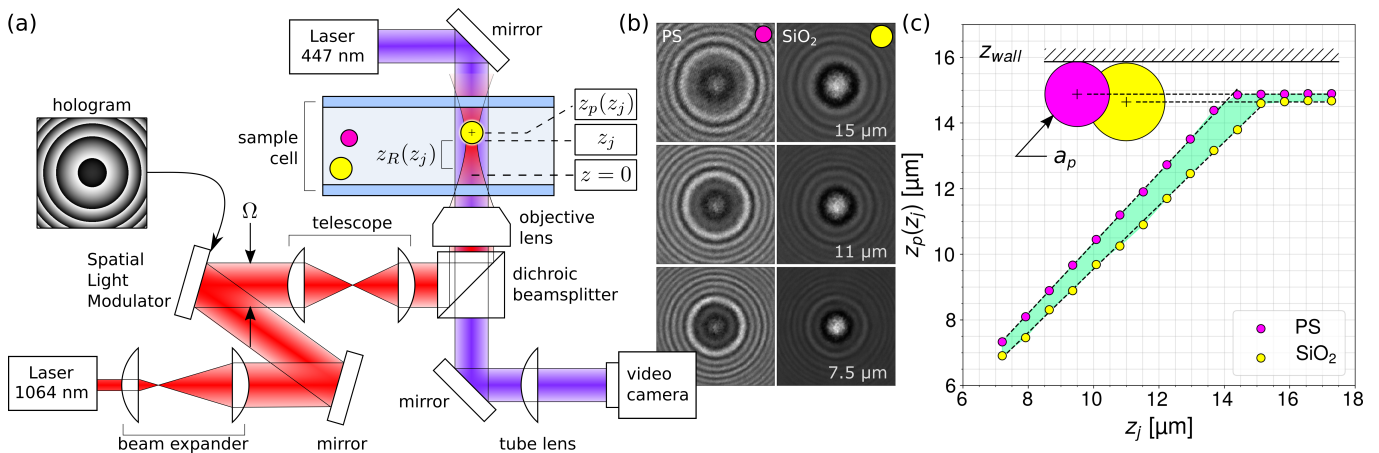


FIG. 1. (a) Schematic representation of the combined instrument for holographic optical trapping and in-line holographic video microscopy. Holographic traps are projected into the sample cell by imprinting a phase hologram onto the wavefronts of an infrared laser beam and relaying the hologram to the input pupil of an objective lens with a dichroic beamsplitter. In-line holograms of trapped particles are recorded with a blue laser beam that passes through the dichroic to a video camera. (b) Typical holograms of a polystyrene sphere (PS) and a silica sphere (SiO₂) displaced to specified axial positions, z_j , by adjusting the phase hologram. (c) Measured axial positions, $z_p(z_j)$, of a polystyrene sphere (PS) and a silica sphere (SiO₂) as a function of specified trap position, z_j . Large circles depict the holographically measured radii, a_p , of the two spheres and are positioned at the measured plateau heights of their trajectories. The two particles thus agree on the height, z_{wall} , of the upper glass wall of their sample cell. Shading between the traces emphasizes the spheres' increasing axial separation.

pressure [16] as well as by external forces such as gravity. Measuring this effect with Lorenz-Mie microscopy [17] not only reveals material-dependent displacements, but also shows that the displacement depends strongly on the trap's axial position, which means that the particle systematically moves either more or less than the trap that is moving it.

LORENZ-MIE MICROSCOPY

The instrument depicted in Fig. 1(a) creates in-line holograms of optically trapped particles [17–19] by illuminating the sample with a collimated laser beam at vacuum wavelength $\lambda_1 = 447$ nm (Coherent Cube) aligned with the optical axis of the objective lens. Light scattered by a particle interferes with the rest of the beam in the focal plane of the objective lens and is relayed by a tube lens to a monochrome video camera (Flir Flea3) that records the intensity of the magnified interference pattern. The imaging subsystem is separated from the trapping subsystem by a dichroic beamsplitter (Semrock). The images in Fig. 1(b) show holograms of a polystyrene sphere and a silica sphere recorded at three different axial displacements, z_j .

Lorenz-Mie microscopy is distinguished from other holographic microscopy techniques by the approach used to extract information from recorded holograms. The incident field is modeled as a monochromatic plane wave linearly polarized along \hat{x} and propagating along $-\hat{z}$:

$$\mathbf{E}_0(\mathbf{r}, t) = E_0 e^{-iqz} e^{-i\omega t} \hat{x}, \quad (4)$$

where $q = 2\pi n_m / \lambda_1$ is the wavenumber of the imaging illumination and $\omega = 2\pi c / \lambda_1$ is its frequency. A particle located at position \mathbf{r}_p within this beam creates a scattered field,

$$\mathbf{E}_s(\mathbf{r}, t) = E_0 e^{-iqz_p} \mathbf{f}_s(q(\mathbf{r} - \mathbf{r}_p)), \quad (5)$$

where $\mathbf{f}_s(q\mathbf{r})$ is the Lorenz-Mie scattering function [20, 21]. If the particle is sufficiently small, the intensity, $I(\mathbf{r})$, recorded at point \mathbf{r} in the camera plane may be modeled as [17]

$$b(\mathbf{r}) = \frac{I(\mathbf{r})}{|E_0|^2} = |\hat{x} + e^{-iqz_p} \mathbf{f}_s(q(\mathbf{r} - \mathbf{r}_p))|^2. \quad (6)$$

For spherical scatterers, the Lorenz-Mie function is parameterized by the sphere's radius, a_p , and its refractive index, n_p . Fitting Eq. (6) pixel-by-pixel to a recorded hologram therefore measures a particle's three-dimensional position and its size while also providing insight into its composition through the refractive index. Published realizations of this technique demonstrate nanometer precision for in-plane tracking, five-nanometer precision for axial tracking, part-per-thousand precision for n_p and five-nanometer precision for a_p [17, 22]. Lorenz-Mie microscopy, moreover, can track a particle as it moves over large axial ranges without requiring mechanical scanning. Comparably good all-optical axial tracking has been achieved with dynamically focused stereomicroscopy [?], which uses a spatial light modulator to maintain a particle in optimal focus. The present study relies on the ability of Lorenz-Mie microscopy to

track particles at different axial positions simultaneously while also measuring their radii and identifying their compositions through their refractive indexes.

The only instrumental calibration constants for Lorenz-Mie microscopy are the vacuum wavelength of the laser, the magnification of the microscope and the refractive index of the medium. Hardware-accelerated computation of the Lorenz-Mie scattering function enables complete fits to be performed in tens of milliseconds [23–25], which is fast enough for interactive operation and instrumental feedback.

ABOVE AND BEYOND: AXIAL DISPLACEMENTS

The representative data plotted in Fig. 1(c) illustrate the challenge posed by axial displacements in holographic optical traps. The two traces show the axial positions of a polystyrene sphere (PS, ThermoFisher Scientific, catalog number 4202A) and a silica sphere (SiO_2 , Bangs Laboratories, catalog number SS05N) localized in water by an optical tweezer and translated straight upward along the optical axis in a sample cell composed of two parallel glass surfaces separated by $15\ \mu\text{m}$. The two spheres were selected from two populations co-dispersed in the same sample at a concentration of 10^5 particles/mL. The polystyrene sphere has a measured radius of $a_p = (0.989 \pm 0.001)\ \mu\text{m}$ and refractive index $n_p = 1.612 \pm 0.001$. The silica sphere has a radius of $a_p = (1.184 \pm 0.031)\ \mu\text{m}$ and refractive index $n_p = 1.396 \pm 0.003$. The two particles are trapped and translated one at a time by the same optical tweezer located at a fixed in-plane position within the sample cell. The trapped sphere is raised in discrete steps of $750\ \text{nm}$. Its characteristics and mean position at each step are obtained by analyzing 50 holograms recorded at 24 frames/s to average over thermal fluctuations. The holograms in Fig. 1(b) show individual snapshots from each of three stages in this process.

The trapped sphere eventually collides with the upper glass wall of the sample cell and so stops rising, even as the trap moves further upward. The height of the plateau augmented by the holographically measured radius of the sphere provides an estimate for the axial position of the wall, $z_{\text{wall}} = \max(z_p(z_j)) + a_p$, as indicated in Fig. 1(c). Although the two spheres' plateau heights differ by $(240 \pm 40)\ \text{nm}$, the associated estimates for z_{wall} differ by just $40\ \text{nm}$, which is comparable to the uncertainty in the radius of the silica particle. Comparably good agreement is obtained consistently with different pairs of particles and usefully validates the precision and accuracy of Lorenz-Mie microscopy for measuring particles' axial positions and radii.

Using z_{wall} as a fiducial point, the substantial difference of $1.2\ \mu\text{m}$ in the spheres' axial positions just before

they reach the wall at $z_j = 14.5\ \mu\text{m}$ cannot be ascribed to measurement error. Instead, this discrepancy shows that the two spheres rise through the cell with significantly different values of the axial scale factor,

$$m_p \equiv \left\langle \frac{dz_p}{dz_j} \right\rangle. \quad (7)$$

The polystyrene sphere rises faster than the trap that is translating it, with $m_p = (1.068 \pm 0.007)\ \mu\text{m}\ \mu\text{m}^{-1}$. The silica sphere sits consistently lower in the trap and moves upward in significantly smaller steps, with $m_p = (0.967 \pm 0.007)\ \mu\text{m}\ \mu\text{m}^{-1}$.

Comparable discrepancies in m_p are observed reproducibly, not just from particle to particle at the same position in the same sample cell, but also from position to position and even in different sample cells. Figure 2(a) presents axial translation data from three types of colloidal spheres measured in multiple sample cells. These samples consist of $1.0\ \mu\text{m}$ -radius polystyrene (PS) spheres, $0.8\ \mu\text{m}$ -radius 3-(trimethoxysilyl)propyl methacrylate (TPM) spheres [25] and $0.8\ \mu\text{m}$ -radius silica (SiO_2) spheres. Each type of sphere translates with a distinctive axial scale factor. The solid lines in Fig. 2(a) represent linear least squares fits whose slopes yield m_p . Their residuals, plotted in Fig. 2(b), display no significant trends.

The axial scale factors from Fig. 2(a) are plotted as crosses in Fig. 2(c), where they are compared with corresponding results from other populations of spheres made of the same three materials. Micrometer-scale spheres made of polystyrene and TPM both rise faster than their traps ($m_p > 1$), with axial scale factors that depend only weakly on size. Silica spheres have axial scale factors that decrease significantly with increasing particle radius, smaller spheres rising faster than their traps and larger spheres rising more slowly.

MODELING AXIAL DISPLACEMENTS

The observed deviations of m_p from unity cannot arise from a simple scaling error because different types of spheres consistently deviate by different characteristic amounts. Nor can these deviations be attributed to aberrations in the trapping beam because both measurements reported in Fig. 1(c) were performed at the same position in the same sample cell, without any intervening mechanical adjustments that could have changed the shape of the trap.

To explain these observations, we model the intensity profile of an optical tweezer as a Gaussian beam brought to a focus at \mathbf{r}_j with intensity profile, $|\mathbf{E}(\mathbf{r} - \mathbf{r}_j)|^2$, given by

$$|\mathbf{E}(\mathbf{r})|^2 = |E_j|^2 \frac{z_R^2}{z^2 + z_R^2} \exp\left(-2\frac{r^2}{w_0^2} \frac{z^2}{z^2 + z_R^2}\right), \quad (8)$$

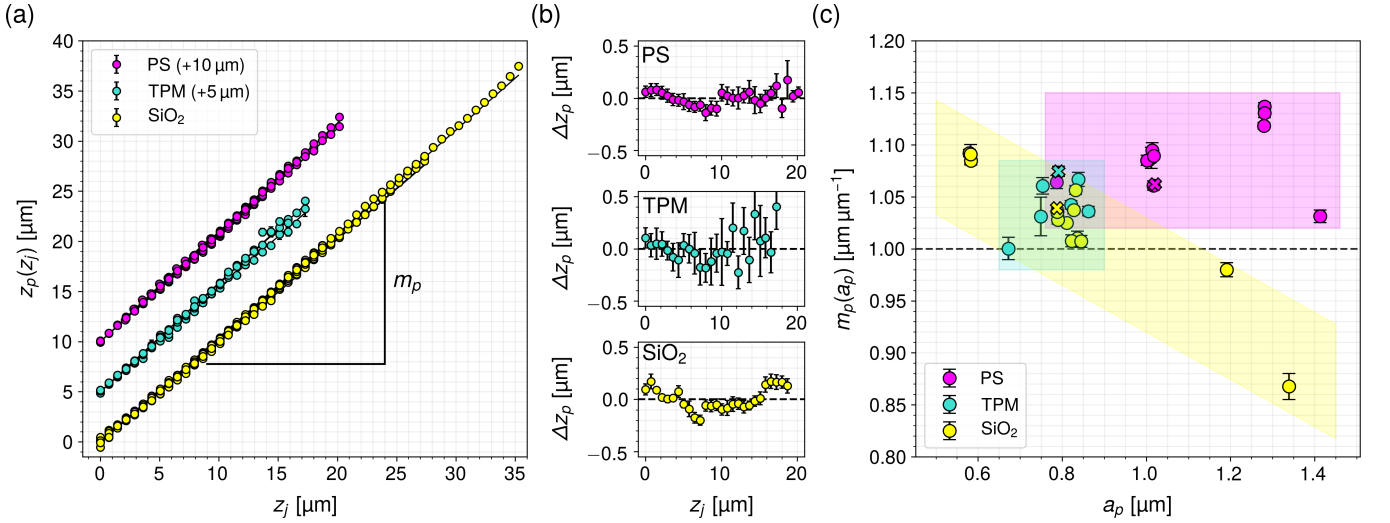


FIG. 2. (a) Axial displacements of colloidal spheres in holographic optical traps, including polystyrene (PS), 3-(trimethoxysilyl)propyl methacrylate (TPM) and silica (SiO₂). Data for polystyrene and TPM are displaced upward for clarity. Each composition is represented by data from multiple spheres (11 for PS, 10 for SiO₂ and 4 for TPM) of nominally identical radii measured in different sample cells. (b) Residuals of displacements from linear fits for each of the three classes of spheres. (c) Experimental measurements of particles' axial scale factors, $m_p(a_p)$, as a function of radius, a_p , for spheres made of polystyrene, silica and TPM. Values from (a) are plotted as crosses.

where $w_0 \approx \lambda_0/(n_m \text{NA})$ is the radius of the beam waist. The axial extent of the focal spot depends on how tightly the beam is focused and is described by the Rayleigh range, z_R . A small particle with complex dipole polarizability $\alpha_e = \alpha'_e + i\alpha''_e$ displaced from the focal point by $\mathbf{r} = (r, \theta, z)$ experiences a dipole-order force [26],

$$\mathbf{F}_e(\mathbf{r}) = -\frac{1}{2} k\alpha'_e |E_j|^2 \left[\frac{r}{z_R} \hat{r} + \frac{z - z_0}{kz_R^2} \hat{z} \right], \quad (9)$$

that draws it toward the axis at a distance,

$$z_0 = \frac{\alpha''_e}{\alpha'_e} z_R (kz_R - 1), \quad (10)$$

downstream of the focal point. This displacement is independent of the trap's intensity, $|E_j|^2$, and reflects a balance between the dipole-order restoring force arising from intensity gradients and radiation pressure directed by phase gradients.

Moving the trap along the axis by z_j changes z_0 by changing the shape of the beam's focus. Specifically, the Rayleigh range depends on z_j as [27]

$$z_R(z_j) = z_R(0) \left(1 + \frac{z_j}{f} \right)^2, \quad (11)$$

where $z_R(0) \approx 8/(k\text{NA}^2)$ sets the scale for a Gaussian beam focused by a lens of numerical aperture NA. The derivation of Eq. (11) requires the Rayleigh range of the beams diffracted by the SLM to be much larger than the focal length of the objective lens, a condition that generally is met in holographic trapping systems.

In the absence of other forces, a trapped particle comes to mechanical equilibrium at

$$z_p(z_j) = z_j + z_0(z_j). \quad (12)$$

Particles therefore tend to be displaced along the optical axis by more than the displacement of the optical trap, with the extra displacement depending on the particle's size and refractive index. The upper trace in Fig. 3 shows $z_0(z_j)$ for a 120 nm-diameter polystyrene sphere in an optical trap modeled by Eq. (8) with parameters for our instrument. Contours of the intensity distribution show that the focal spot expands along the axial direction as z_j increases, thereby increasing the particle's displacement from the focal point.

Displacing a trap along the axial direction decreases its stiffness through the dependence of $\mathbf{F}_e(\mathbf{r})$ on z_R , as shown approximately in Eq. (9). The scale of a trapped particle's thermal fluctuations about $z_p(z_j)$ therefore should increase as z_j increases. This trend is reflected in the increasing standard deviation of $\Delta z_p(z_j)$ plotted in Fig. 2(b).

For displacements smaller than the focal length of the objective lens, $z_j < f$, the dependence of z_p on z_j is roughly linear and is characterized by the axial scale factor

$$m_p \approx 1 + 2 \frac{\alpha''_e}{\alpha'_e} \frac{z_R(0)}{f} [2kz_R(0) - 1]. \quad (13)$$

For our instrument, $m_p \approx 1 + 0.037 \frac{\alpha''_e}{\alpha'_e}$. Observing the nonlinear scaling predicted by Eqs. (10) through (12) is not feasible because particles escape their traps when

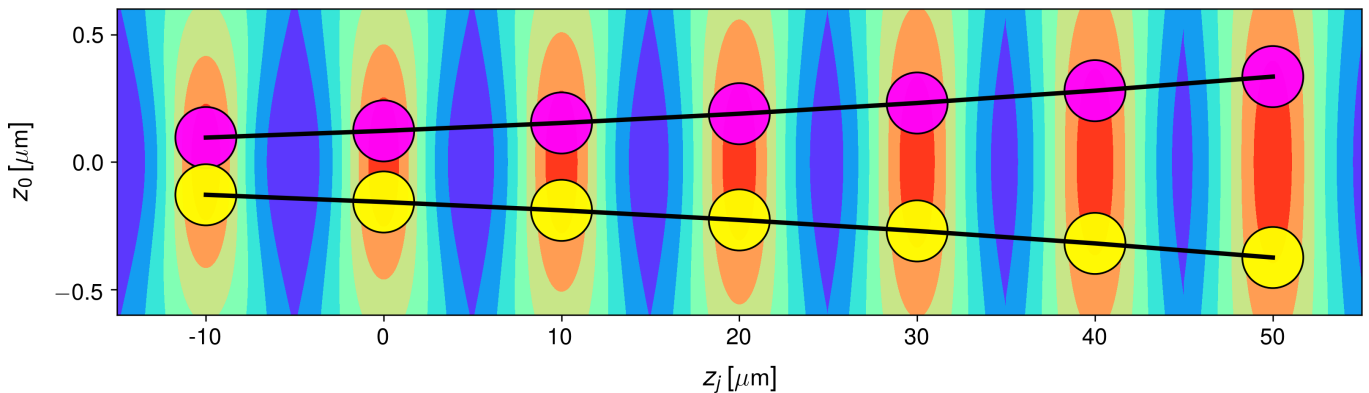


FIG. 3. Particle position, z_0 , within an optical trap as a function of the trap's axial displacement, z_j for 120 nm-diameter polystyrene (PS, magenta, upper) and silica (SiO_2 , yellow, lower) spheres dispersed in water and trapped in a diffraction-limited optical tweezer at $\lambda_0 = 1064$ nm. Colored contours reveal how the trap's intensity profile, $|\mathbf{E}(\mathbf{r})|^2$, broadens and elongates with increasing z_j . The polystyrene sphere rises in the trap, while the silica sphere sinks.

$z_0(z_j)$ becomes large. Indeed, material-dependent displacements set an upper limit on the axial range through which colloidal particles can be translated with holographic optical tweezers.

For the particular case of a small dielectric sphere of radius a_p and refractive index n_p immersed in a medium of refractive index n_m , the electric dipole polarizability is [28]

$$\alpha_e = \frac{\alpha_e^{(0)}}{1 - \frac{i}{6\pi\epsilon_0 n_m^2} k^3 \alpha_e^{(0)}}, \quad (14)$$

where the Clausius-Mossotti polarizability is

$$\alpha_e^{(0)} = 4\pi\epsilon_0 n_m^2 a_p^3 \frac{n_p^2 - n_m^2}{n_p^2 + 2n_m^2}. \quad (15)$$

Given this, a sphere's axial scale factor depends on its radius, a_p , and refractive index, n_p , through the ratio

$$\frac{\alpha_e''}{\alpha_e'} \approx \frac{2}{3} (ka_p)^3 \frac{n_p^2 - n_m^2}{n_p^2 + 2n_m^2}. \quad (16)$$

Small, weakly scattering particles therefore tend to be localized near the focal points of their traps. Variability in axial placement becomes more of an issue for larger particles with larger index mismatches.

Equation (16) is valid for particles that are substantially smaller than the wavelength of light $ka_p < 1$. Holographic tracking and characterization, however, requires particles that are larger than the wavelength of light. The data for polystyrene and TPM in Fig. 2(c) therefore all have $ka_p > 1$ and show a comparatively weak dependence on particle size, presumably because the particles are larger than the radius of the beam waist, $w_0 \approx 550$ nm.

The data for silica spheres in Fig. 2(c) show a downward trend in $m_p(a_p)$ that runs counter to the prediction of Eq. (13) and can be explained by the influence of gravity. The weight of a sphere of density ρ_p dispersed in a

fluid of density ρ_m shifts the point of mechanical equilibrium by a distance

$$\Delta z_0(z_j) = -\frac{8}{3} \pi a_p^3 (\rho_p - \rho_m) g \frac{z_R^2(z_j)}{\alpha_e' |E_j|^2}, \quad (17)$$

where g is the acceleration due to gravity. This offset depends on axial displacement through the dependence of z_R on z_j , and thus affects the axial scale factor, m_p . The lower trace in Fig. 3 shows how the axial displacement of a 120 nm-diameter silica sphere depends on trap position given the combination of optical and gravitational forces. Unlike the neutrally-buoyant polystyrene sphere ($\rho_p = 1.05 \text{ g cm}^{-3}$) the dense silica sphere ($\rho_p = 2 \text{ g cm}^{-3}$) lags behind the focal point as the trap moves upward. TPM has an intermediate refractive index ($n_p = 1.5$) and an intermediate density ($\rho_p = 1.23 \text{ g cm}^{-3}$) and so is predicted to have an intermediate displacement.

Equation (17) is valid for particles whose density mismatch is small enough that $z_0 + \Delta z_0 < z_R$. Within this range, Eqs. (14), (15) and (17) suggest that Δz_0 depends only weakly on a_p . In fact, the data for silica spheres in Fig. 2(c) shows that gravity causes larger spheres to sit lower in their traps and to rise more slowly. This is consistent with the observation of weaker-than-predicted size scaling for comparably sized polystyrene and TPM spheres. Although the dipole-order theory accounts for qualitative features of the observed displacements, quantitative predictions for larger spheres presumably require a higher-order treatment. Limitations of the analytically tractable dipole-order theory highlight the value of holographic microscopy for providing *in situ* experimental feedback, particularly for particles that are larger than the wavelength of light.

DISCUSSION

We have used Lorenz-Mie microscopy to demonstrate that holographically trapped colloidal spheres are displaced within their traps by amounts that depend substantially on the traps' axial positions. These displacements, often amounting to more than the wavelength of light, are explained by changes in the traps' Rayleigh ranges as they move along the optical axis. How this affects the position of a particle within a trap depends on the particle's size and refractive index, and also can be influenced by external forces such as gravity. Whereas in-plane displacements can be measured and calibrated with conventional microscopy and standard techniques of image analysis [29], axial displacements have been much more challenging to measure and so have been largely overlooked. The present study demonstrates that ignoring material-dependent axial displacements can lead to large errors in particle placement, not only for heterogeneous assemblies, but also for nominally identical spheres arranged in three-dimensional patterns. The comparative difficulty of predicting and correcting these offsets *a priori* creates a need for the real-time feedback that can be provided by quantitative holographic video microscopy.

FUNDING

This work was supported by the MRSEC program of the National Science Foundation through Award Number DMR-1420073. The instrument used for this work was constructed with support of the MRI program of the NSF under Award Number DMR-0922680. We gratefully acknowledge the support of the nVidia Corporation through the donation of the Titan Xp GPU used for this research.

-
- [1] Eric R. Dufresne and David G. Grier, "Optical tweezer arrays and optical substrates created with diffractive optical elements," *Rev. Sci. Instrum.* **69**, 1974–1977 (1998).
- [2] David G. Grier, "A revolution in optical manipulation," *Nature* **424**, 810–816 (2003).
- [3] Yael Roichman and David G. Grier, "Holographic assembly of quasicrystalline photonic heterostructures," *Opt. Express* **13**, 5434–5439 (2005).
- [4] Stephen C. Chapin, Vincent Germain, and Eric R. Dufresne, "Automated trapping, assembly, and sorting with holographic optical tweezers," *Opt. Express* **14**, 13095–13100 (2006).
- [5] DC Benito, DM Carberry, SH Simpson, GM Gibson, MJ Padgett, JG Rarity, MJ Miles, and S Hanna, "Constructing 3D crystal templates for photonic band gap materials using holographic optical tweezers," *Opt. Express* **16**, 13005–13015 (2008).
- [6] Jennifer E. Curtis, Brian A. Koss, and David G. Grier, "Dynamic holographic optical tweezers," *Opt. Commun.* **207**, 169–175 (2002).
- [7] Marco Polin, Kosta Ladavac, Sang-Hyuk Lee, Yael Roichman, and David G. Grier, "Optimized holographic optical traps," *Opt. Express* **13**, 5831–5845 (2005).
- [8] Yohai Roichman and David G. Grier, "Projecting extended optical traps with shape-phase holography," *Opt. Lett.* **31**, 1675–1677 (2006).
- [9] Yohai Roichman, Ilias Cholis, and David G. Grier, "Volumetric imaging of holographic optical traps," *Opt. Express* **14**, 10907–10912 (2006).
- [10] Yohai Roichman and David G. Grier, "Three-dimensional holographic ring traps," *Proc. SPIE* **6483**, 64830F (2007).
- [11] Elisabeth R. Shanblatt and David G. Grier, "Extended and knotted optical traps in three dimensions," *Opt. Express* **19**, 5833–5838 (2011).
- [12] José A. Rodrigo, Tatiana Alieva, Eugeny Abramochkin, and Izan Castro, "Shaping of light beams along curves in three dimensions," *Opt. Express* **21**, 20544–20555 (2013).
- [13] Sang-Hyuk Lee, Yohai Roichman, and David G. Grier, "Optical solenoid beams," *Opt. Express* **18**, 6988–6993 (2010).
- [14] David B. Ruffner and David G. Grier, "Optical conveyors: A class of active tractor beams," *Phys. Rev. Lett.* **109**, 163903 (2012).
- [15] S Bianchi and Roberto Di Leonardo, "Real-time optical micro-manipulation using optimized holograms generated on the GPU," *Computer Physics Communications* **181**, 1444–1448 (2010).
- [16] A. Ashkin, J. M. Dziedzic, J. E. Bjorkholm, and S. Chu, "Observation of a single-beam gradient force optical trap for dielectric particles," *Opt. Lett.* **11**, 288–290 (1986).
- [17] Sang-Hyuk Lee, Yohai Roichman, Gi-Ra Yi, Shin-Hyun Kim, Seung-Man Yang, Alfons van Blaaderen, Peter van Oostrum, and David G. Grier, "Characterizing and tracking single colloidal particles with video holographic microscopy," *Opt. Express* **15**, 18275–18282 (2007).
- [18] Jian Sheng, Edwin Malkiel, and Joseph Katz, "Digital holographic microscope for measuring three-dimensional particle distributions and motions," *Appl. Opt.* **45**, 3893–3901 (2006).
- [19] Sang-Hyuk Lee and David G. Grier, "Holographic microscopy of holographically trapped three-dimensional structures," *Opt. Express* **15**, 1505–1512 (2007).
- [20] Craig F. Bohren and Donald R. Huffman, *Absorption and Scattering of Light by Small Particles* (Wiley Interscience, New York, 1983).
- [21] M. I. Mishchenko, L. D. Travis, and A. A. Lacis, *Scattering, Absorption and Emission of Light by Small Particles* (Cambridge University Press, Cambridge, 2001).
- [22] Bhaskar Jyoti Krishnatreya, Arielle Colen-Landy, Paige Hasebe, Breanna A. Bell, Jasmine R. Jones, Anderson Sunda-Meya, and David G. Grier, "Measuring Boltzmann's constant through holographic video microscopy of a single sphere," *Am. J. Phys.* **82**, 23–31 (2014).
- [23] Fook Chiong Cheong, Bo Sun, Rémi Dreyfus, Jesse Amato-Grill, Ke Xiao, Lisa Dixon, and David G. Grier, "Flow visualization and flow cytometry with holographic video microscopy," *Opt. Express* **17**, 13071–13079 (2009).
- [24] Aaron Yevick, Mark Hannel, and David G. Grier, "Machine-learning approach to holographic particle characterization," *Opt. Express* **22**, 26884–26890 (2014).

- [25] Mark D. Hannel, Aidan Abdulali, Michael O'Brien, and David G. Grier, "Machine-learning techniques for fast and accurate feature localization in holograms of colloidal particles," *Opt. Express* **26**, 15221–15231 (2018).
- [26] Aaron Yevick, Daniel J. Evans, and David G. Grier, "Photokinetic analysis of the forces and torques exerted by optical tweezers carrying angular momentum," *Phil. Trans. Roy. Soc. A* **375**, 20150432 (2017).
- [27] Sidney A. Self, "Focusing of spherical Gaussian beams," *Appl. Opt.* **22**, 658–661 (1983).
- [28] B. T. Draine and Jeremy Goodman, "Beyond Clausius-Mossotti: Wave propagation on a polarizable point lattice and the discrete dipole approximation," *Astrophys. J.* **405**, 685–697 (1994).
- [29] John C. Crocker and David G. Grier, "Methods of digital video microscopy for colloidal studies," *J. Colloid Interface Sci.* **179**, 298–310 (1996).